Photoelectrocatalytic Degradation of Emerging Contaminants at WO_3/$BiVO_4$ Photoanodes in Aqueous Solution.

Vito Cristino[a], Luisa Pasti[a]*, Nicola Marchetti[a], Serena Berardi[a], Carlo Alberto Bignozzi[a] Alessandra Molinari[a], Francesco Passabi[a], Stefano Caramori*[a], Lucia Amidani[b], Alberto Piccioni[c], Jagadesh Kopula Kesavan[c], Federico Boscherini[c] and Luca Pasquini[c]

(a) Department of Chemical and Pharmaceutical Sciences, University of Ferrara, Via L. Borsari 46, 44121 Ferrara, Italy.

(b) Helmholtz-Zentrum dresedn-Rossendorf, c/o European Synchrotron Radiation Facility, 71 Avenue des Martyrs, 38000 Grenoble, France.

(c) Department of Physics and Astronomy, University of Bologna, Viale C. Berti Pichat 6/2, 40127, Bologna, Italy.

Abstract

WO_3/$BiVO_4$ films obtained by electrochemical deposition of $BiVO_4$ over mesoporous WO_3 were applied to the photoelectrochemical degradation of selected emerging contaminants (ketoprofen and levofloxacine) in aqueous solution. WO_3/$BiVO_4$ films of this work are characterized by a mesoporous morphology with a maximum photoconversion efficiency > 40 % extending beyond 500 nm in Na_2SO_4 electrolytes. Oxygen was found the dominant water oxidation product (ca. 90 % Faradaic yield) and no evidence for the photogeneration of OH radicals was obtained. Nevertheless, both 10 ppm levofloxacine and ketoprofen could be degraded at $BiVO_4$ junctions upon a few hours of illumination under visible light. However, while levofloxacine degradation intermediates were progressively consumed by further oxidation at the WO_3/$BiVO_4$ interface, ketoprofen oxidation byproducts, being stable aromatic species, were found to be persistent in aqueous solution even after 15 hours solar simulated illumination. This indicates that, due to the lower oxidizing power of photogenerated holes in $BiVO_4$ and to a different water oxidation mechanism, the employment of WO_3/$BiVO_4$ in photoelectrochemical environmental remediation processes is much less universal than that possible with wider band gap semiconductors like TiO_2 and WO_3.

1. Introduction

$BiVO_4$ is an intermediate band gap semiconductor object of intense research in the field of photoelectrochemistry, solar energy conversion/ storage and photocatalysis, mainly owing to its visible absorption - extending up to 500 nm - associated to direct electronic transitions from valence to conduction band edges, energetically positioned to drive many interesting redox reactions.[1] In addition to the former intrinsic properties, a number of potentially scalable electrochemical and wet chemical preparation routes to $BiVO_4$ and its modification are available, adding flexibility to the employment of such material for energy related applications.[2, 3, 4] From

the electronic point of view,[5] the valence band of $BiVO_4$ bears a dominant contribution from oxygen 2p states and a strong component (ca. 18 %) from Bi 6s orbitals, while the conduction band is constituted by rather localized V 3d orbitals mixed with the O ones. This results in a sharp density of states (DOS) of the conduction band, associated to high electron effective mass and poor mobility. On the other hand, based on the computed DOS diagram, the mobility of holes at the valence band edge should be larger. Due to the general need of maximizing the interfacial area of the photocatalyst for substrate adsorption and redox reactions and to its intrinsic electronic properties, most of the applications of $BiVO_4$ involve i) the fabrication of nanostructured morphologies whose size should be as much compatible as possible with the expected short diffusion length of the charge carriers ii) the formation of heterointerfaces which can improve charge separation via interfacial charge transfer.

In the framework of photocatalysis, metal modified $BiVO_4$ nanoparticles were applied to the degradation of pollutants like chloro-phenols and of model organic dyes like methylene blue[6] in aqueous solution, with evidence of production of a small EPR signal assigned to formation of OH radicals under visible light illumination. Nevertheless, the need for optimizing interfacial charge separation in pure $BiVO_4$ was addressed by Castillo et al.[7] who could observe the degradation of phenol and chloroacetic acid only in the presence of a well-defined concentration of H_2O_2 acting as a sacrificial scavenger of both electrons and holes. In this specific case, the facile reduction of H_2O_2 by photogenerated electrons could lead to the production of OH radicals, acting as powerful oxidizing intermediates. The photocatalytic degradation of phenols was investigated by Long et al.[8] by using $Co_3O_4/BiVO_4$ composite nanoparticles observing enhanced efficiency over unmodified $BiVO_4$, attributed to the formation of a local p-n junction instrumental in reducing photocarrier recombination within those nanoparticles. A similar mechanism was postulated by Shang et al.[9] in evaluating the photocatalytic degradation of model dyes with $BiVO_4$/PANI (PANI=polyaniline) particles. The efficiency of the electron transfer between the different phases of the heterojunction seems to be critically dependent on local band alignment and facets orientation; better charge separation was observed at $BiVO_4/TiO_2$ n-n heterojunctions[10] as well as in the presence of different co-catalysts decorating selected facets of $BiVO_4$ nanocrystals[11].

Some authors developed a Z scheme photocatalyst based either Ag/AgCl modified $BiVO_4$ [12]or AgI/$BiVO_4$[13] which was demonstrated comparatively effective over unmodified $BiVO_4$ in the photodegradation of Rhodamine B and tetracycline respectively; Li et al.[12] also exploited their Ag/AgCl/$BiVO_4$ composite to fabricate photoelectrodes, however the resulting

photoelectrochemical performance was less than optimal compared to Ag^+ modified $BiVO_4$ thin films fabricated to the aim of solar energy conversion.[14]

The photoelectrocatalytic conditions, i.e. the exploitation of semiconductor photoelectrodes in an electrochemical cell in the presence of electrochemical polarization,[15-17] could indeed offer advantages over conventional open circuit photocatalysis, such as: 1) the applied potential regulates and optimizes charge separation, without requiring the use of sacrificial species; 2) the two distinct processes of oxidation (due to photogenerated holes) and reduction (due to photogenerated electrons) can be carried out at separated compartments of the photoelectrochemical cell, simplifying, in the case of formation of chemically valuable products (photoelectrosynthetic cells), (ref, Meyer e Springer) their separation; 3) the catalyst, either in the form of a solid electrode, or solidly attached to an ohmic conductor, can be easily retrieved from the solution, avoiding accidental contamination of water with catalyst (nano)particles; 4) polarization can tune adsorption and promote the reaction of otherwise untreatable contaminants, as recently shown in the case of the degradation of ketoprofen at illuminated WO_3 thin films.[18] The price to pay for the former potential advantages consists, commonly, in a more complex setup and in the need to optimize photoelectrode performance added to the less effective physical contact between the photocatalyst and the target species. It is a well-known fact that mass transport is easier in disperse systems than in a photoelectrochemical cell where redox reactions may occur only at the photoelectrode/solution interface. Ostensibly due to these reasons, the photoelectrocatalytc degradation of real contaminants with $BiVO_4$ based materials has been generally less studied: Zhou et al.[19] explored the photoelectrocatalytic degradation of phenols at $BiVO_4$ photoelectrodes, finding that a nearly complete oxidative degradation, al least of the parent compounds, could be achieved after 5 hours illumination. The reported photoelectrochemical performance was however quite modest, with photocurrents less than 100 $\mu A/cm^2$, meaning that charge recombination within those $BiVO_4$ photoanodes was largely limiting the degradation efficiency. The photoelectrocatalytic degradation of dyes under visible illumination at $WO_3/BiVO_4$ heterojunctions[20-22] was later explored by Chatchai et al.,[23] but the performance of the reported photoelectrochemical cell based on a $(WO_3/BiVO_4)$n-p(Cu_2O) architecture was again rather low with a limiting photocurrent of the order of 0.01 mA/cm^2 at 0.8 V.

Herein, we explore the photoelectrochemical properties of optimized colloidal $WO_3/BiVO_4$ junctions, delivering performances comparable to the current state of the art for equivalent materials for energy applications[24, 25] to the aim of exploring their efficiencies in the decontamination of water from emerging organic contaminants. In particular, after the characterization of the photoelectrochemical properties of these junctions in different electrolytes, we will focus on the

degradation kinetic of ubiquitous contaminants of emerging concern, i.e. Ketoprofene[26] (KTP) and Levofloxacine[27] (LFX) (chart 1) and on the detailed characterization of the chemical nature and of the fate and of their degradation intermediates generated under photoelectrochemical (applied electrical bias) conditions, in order to obtain insights about their degradation pathway at $WO_3/BiVO_4$ junctions.
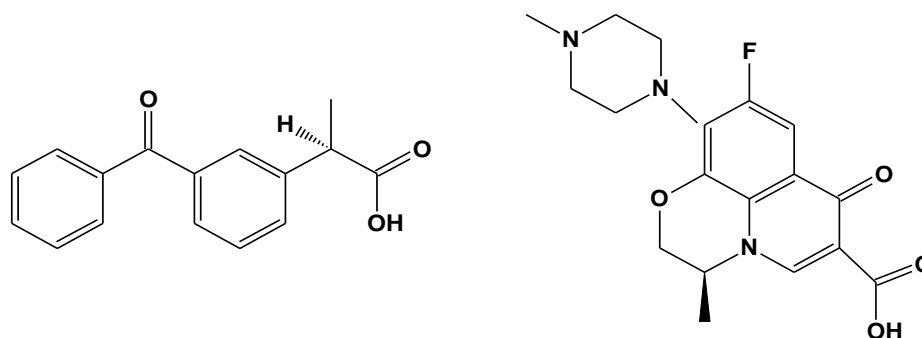

Chart 1. Molecular structures of KTP (left) and LFX (right). Both molecules are represented in their neutral form.

2. Experimental

2.1 Chemicals for Analytical and Photoelectrochemical experiments: Levofloxacin (Fluka, purity >98%), ketoprofen (Sigma-Aldrich, purity >98%), sodium sulfate (Sigma-Aldrich, purity, 99%), sulfuric acid (Sigma-Aldrich, 95%), 1 M phosphate buffer (pH 7.4, Sigma-Aldrich) and 0.5 M borate buffer (pH 9, Alfa), Na_2SO_4 (Fluka, 99%), K_2IrCl_6 (33.4 % Ir, Alfa Aesar), sodium acetate (Riedel de Häen 99 %), 70 % HNO_3 (Sigma-Aldrich), V_2O_5 (Alfa Aesar 99.6 %), $VOSO_4 \times x\ H_2O$ (Alfa Aesar, 99.9 %), $Bi(NO_3)_3 \times 5\ H_2O$ (Alfa Aesar 99.99 %), methanol, formic acid, sodium hydroxide, sodium citrate, High-Performance Liquid Chromatography (HPLC) grade acetonitrile (ACN) was purchased from Merck (Darmstadt, Germany). The water was Milli-Q® grade (Millipore, MA, USA). High-performance liquid chromatography (HPLC) grade acetonitrile (ACN) was purchased from Merck (Darmstadt, Germany). The water was Milli-Q® grade (Millipore, MA, USA).

When necessary, a dilute aqueous solution of sulfuric acid was employed to adjust at 6 the pH of the drug solution (10 ppm Levofloxacin or Ketoprofen) containing 0.7mM of sodium sulfate as supporting electrolyte. The saline concentration was chosen to reproduce the average salinity of freshwater.[28] The pH of the drug solutions was measured with a combined glass electrode connected to an AMEL pH-meter (Milano, Italy).

2.2 Preparation of transparent thin film photoelectrodes for photoelectrocatalysis

Nanocrystalline WO_3 on FTO was prepared by following a published procedure.[29] Deposition of $BiVO_4$ on WO_3 was carried out by a slight modification of a potentiostatic procedure originally proposed by Seabold.[30] Briefly, 10 mM $VOSO_4$ in millipore water is acidified by addition of HNO_3 up to pH 0.5 followed by addition of 10 mM $Bi(NO_3)_3$. Further HNO_3 is added until $Bi(NO_3)_3$ is completely dissolved. After this point the pH is quickly raised to 4.5 by using 2 M CH_3COONa. This solution is rapidly used (to avoid excessive hydrolysis and precipitation of Bi^{3+} compounds) for two electrode potentiostatic electrodeposition by applying 210 mV between FTO/WO_3 and a platinum foil for 600 s at room temperature. Alternatively, a potential of 1 V could be applied against a Ti sheet for 300 s with equivalent results. For electrodeposition, the counter electrode is cofacially assembled with the photoanode, held at ca. 3 mm distance. An intense yellow/orange coloration of the photoanode is observed after this stage. The resulting substrates are thoroughly rinsed with Millipore water and annealed at 500 °C for 2 hours in order to form nanocrystalline $BiVO_4$ in monoclinic form, as confirmed by grazing angle XRD diffraction (Figure S1) and by absorption spectra (see below). The resulting thin films show, at the naked eye, good homogeneity and transparency (Figure 1). Basic NaOH post treatment finalized to remove V_2O_5 were not applied. No V_2O_5 was observed from XRD nor photoelectrochemical improvement was recorded with the photoanodes after the initial treatments with basic baths, which were then soon abandoned.

$BIVO_4$ powder for EPR spectroscopy was prepared by reacting 50 mM $Bi(NO_3)_3$ with 50 mM V_2O_5 in 2 M HNO_3 at ca. 100 °C until precipitation of a red compound was observed. The precipitate is removed by filtration, washed with water, dried in an oven and finally fired at 500 C° for 2 hours in air, leading to yellow $BiVO_4$.
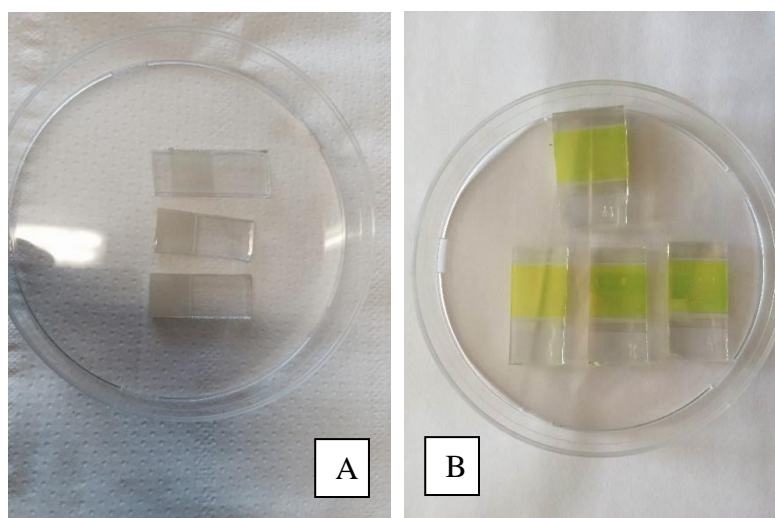

Figure 1. WO_3 Photoanodes before (A) and after (B) $BiVO_4$ deposition and annealing. Geometric active area of semiconductor thin film electrodes is 1 cm^2

2.3 AFM

Atomic force microscopy (AFM) images were collected using a Digital Instruments Nanoscope III scanning probe Microscope (Digital Instruments, CA). The instrument was equipped with a silicon tip (RTESP-300 Bruker) and operated in tapping mode. Surface topographical analysis of AFM images was carried out with NanoScope analysis 1.5

2.4 X-Ray Spectroscopy

X-ray spectroscopy measurements were performed at the ID26 beamline of the ESRF, Grenoble, France. High energy resolution fluorescence detected (HERFD)-XANES spectra at the V K-, Bi L_3- and W L_3-edges were obtained exploiting the Rowland circle based emission spectrometer of the beamline. Crystal analyzers were Ge (331), Ge(844) and Si(551) for V, Bi and W edge spectra, respectively. For the simulations the atomic coordinates of the unit cell of monoclinic $BiVO_4$ and triclinic WO_3 were generated by VESTA software, using the cif file taken from the American Mineralogist Crystal Structure Database[31] and then used as input for the FDMNES code[32] to calculate the XANES spectra; again, the simulations are relative to the total X-ray absorption spectra (non-high resolution XANES). Convolution by a lorentzian, whose width increases versus energy as an arctangent function with the default FDMNES parameters and a few eVs shift in order to align the edges have been applied to the simulations after the calculations.

2.5 Photoelectrochemical characterization.

Potentiodynamic J-V curves were carried out in a three electrode cell using platinum as counter electrode and an SCE as reference electrode. The typical scan rate was 10 mV/s. Clark-type (Crison OXI 45 + equipped with a 51 20 sensor) oxygen detection experiments were carried out under galvanostatic conditions (current = 0.5 mA/cm^2) and compared to IrO_x electrodes biased at the same. IrOx substrates were obtained by drop casting a 2×10^{-3} M K_2IrCl_6 solution on FTO followed by annealing at 450 °C in air. Oxygen detection experiments based on generation/collection experiments were performed with a sandwich thin layer cell in a bipotentiostatic arrangement described elsewhere[33, 34] by using the $WO_3/BiVO_4$ photoanode as the oxygen generator and FTO as the oxygen collector. Incident Photon to Current Conversion Efficiency (IPCE) measurements were performed under constant potential with a previously described setup.

2.6 Photo-electrochemical degradation experiments

Photodegradation experiments under photo-electrochemical conditions were carried out in a two electrode cell (volume = 10 mL) under potentiostatic conditions controlled by an Eco Chemie

PGSTAT 101 potentiostat/galvanostat running under Nova environment. The working electrode (photoanode) was $WO_3/BiVO_4$ thin film supported on FTO, while the counter electrode was a platinum grid. An ABET sun simulator (Air Mass (AM) 1.5 G with the appropriate cut offs) was used as an illumination source for photoelectrochemical experiments. Constant potential photoelectrolysis was conducted in a two electrode cell in both aerated 0.1 M and 0.7 mM Na_2SO_4 aqueous solutions at, respectively pH 7 and pH 6 by applying a constant bias of 1.2 V for KTP and either 1.5 or 0.4 V for LFX. Typical experiments had a duration of 5 hours, during which depolarization cycles at 0 V for 10 minutes were introduced between polarization cycles of the duration of 30 minutes in order to ensure a reproducible and stable operation of the photoelectrode. Longer experiments, aimed at the determination of decomposition intermediates were carried out for 16 hours, by adopting the same electrochemical program specified above.

2.7 Electron Paramagnetic Resonance

EPR spin-trapping experiments were carried out with a Bruker MRD spectrometer equipped with a TE 201 resonator (microwave frequency of 9.4 GHz, center field 3460 G, receiver gain $2x10^5$, time constant 40,96 s). The samples were aqueous suspensions of $BiVO_4$ containing $NaClO_4$ (0.1M, at pH 6-7) and 5,5 dimethyl-pyrrolin N-oxide (DMPO, 5 10^{-2} M) as the spin trap. The samples were put into a flat quartz cell and directly illuminated in the instrument cavity by a Hg medium pressure lamp. Selected cut-off filters (λ> 450, 420, 380, 360) were put between the lamp and the cell. When requested α-phenyl N-tert-butyl nitrone (pbn, $5x10^{-2}$ M) has been used in place of DMPO. Analogous experiments were performed substituting $BiVO_4$ with suspended WO_3.

2.7 HPLC/DAD analysis

A HPLC/DAD (Waters, MA, USA pump:Waters 515, DAD:Waters PDA 996) was employed under isocratic elution condition, the eluent was 18:82 ACN: phosphate buffer 25 mM at pH 4 and 60:40 MeOH: phosphate buffer 2mM at pH 3.3 for LFX and KTP respectively. The flow rate was 1 mL/min. The column was 4.6x150 mm Kromasil Eternity-5-C18. The injection volume was 20 µL for all standards and samples.

2.8 HPLC/MS analysis

HPLC/MS analyses were made by means of Surveyor micro-HPLC hyphenated to a linear trap quadrupole mass spectrometer (LTQ XL Thermo Scientific, Waltham, MA, USA). The HPLC apparatus was composed of a solvent delivery system, a quaternary pump (including a membrane degasser) and an autosampler (including a thermostated column compartment). The LTQ system was equipped with an electrospray ionization (ESI) ion source. The mobile phase was obtained as a

mixture of acetonitrile (ACN) formic acid 0.1% v/v : water formic acid 0.1% v/v. Chromatographic separation was performed under gradient elution conditions: 0-6 min 5% ACN, 6-14 min 5-70% ACN, 14-15 min 70% ACN, then held isocratically at 95% of ACN for 3 min before reconditioning the column. The flow rate was 100 μL/min, while the column was thermostated at 25 °C. The column was 50 x 2.1 mm (Restek, Bellefonte, PA, USA) and packed with a C18 silica-based stationary phase with a particle diameter of 3 μm. The injection volume was 5 μL for all standards and samples. MS experimental conditions were as follows: spray voltage 4 kV, capillary temperature 275 °C, capillary voltage 11 V and tube lens 25 V for positive ESI conditions.

3. Results and Discussion

3.1. Morphological, Structural and Spectral properties of WO$_3$/BiVO$_4$ heterojunctions

Figure 2 reports the absorption spectra of the WO$_3$/BiVO$_4$ photoanodes, compared to WO$_3$ films. Following BiVO$_4$ deposition it can be observed a generalized increase in optical density starting from ca. 490 nm and reaching 2.5 absorbance units in the UV region, where one sums the absorption of both WO$_3$ and BiVO$_4$. Compared to pristine WO$_3$, whose absorption does not extend beyond 450 nm (the 450 nm hump is an absorption artifact probably related to FTO and always present when recording WO$_3$ spectra in transmission mode)[29] and is already very small at ca. 420 nm. The n-n junction covers a range between 450 and 400 nm where its Light Harvesting Efficiency (LHE (λ)=1-$10^{-A(\lambda)}$ where A is the film absorbance) is close to unity. The absorption spectrum of WO$_3$/BiVO$_4$ confirms the presence of the monoclinic phase of BiVO$_4$ exhibiting a band gap of ca. 2.4 eV according to Kudo et al.[35] and this finding is consistent with XRD results of Figure S1 where one can observe, in the thin film, the simoultaneous presence of diffraction peaks assigned to monoclinic WO$_3$, monoclinic BiVO$_4$ and FTO (tetragonal F doped SnO$_2$). It has been reported that the monoclinic phase of BiVO$_4$ has the best performances in photocatalytic oxygen evolution upon visible light excitation ,[36] therefore, it is the desired one for our intended application.
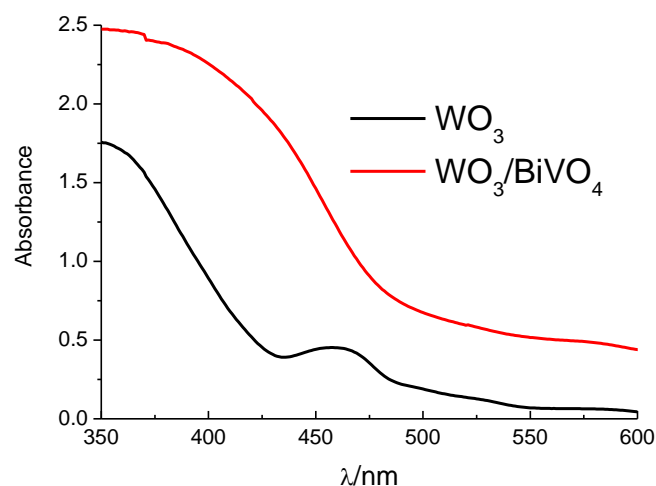
Figure 2. Absorption spectra, recorded in transmission mode, of WO_3 (black) and $WO_3/BiVO_4$ photoanodes

In order to evaluate whether the local atomic environment of V, Bi and W in the synthesized samples reflects the local structure of these elements in $BiVO_4$ and WO_3 stoichiometric bulk compounds a comparison with literature data and *ab initio* simulations of XANES spectra were performed (Figure 3). As for the comparison with literature data it must be mentioned that published spectra are relative to the total X-ray absorption cross section measured in the conventional, non-high resolution mode. In Figure 1 the V K -, Bi L_3 - and W L_3 - edge spectra are compared with the corresponding *ab-initio* calculated spectra and to literature data (V^{37}, Bi^{38}, W^{39}). Overall, the comparison between recorded, simulated and reference spectra is very convincing. In particular, for the V edge spectrum there is a good agreement of all spectral features between the experimental, literature and simulated spectra. The intensity of the pre-edge feature due to a 1*s* to 3*d* transition (allowed by 3*d*–4*p* orbital hybridization)[37] is well reproduced by the simulations while its position is slightly offset. For the W and Bi L_3 edge spectra there is again good agreement; we note that, thanks to the high resolution of the measurement technique, the ligand – field splitting of the final states (t_{2g} and e_g)[39] is much more evident in our experimental HERFD-XANES spectra than in the literature and simulation XANES ones.

The agreement between experimental data, calculated and reference spectra is clearly evident, confirming that the local atomic structure of V, Bi and W in the synthesized samples reflects the typical local structure of these compounds in their stoichiometric form.
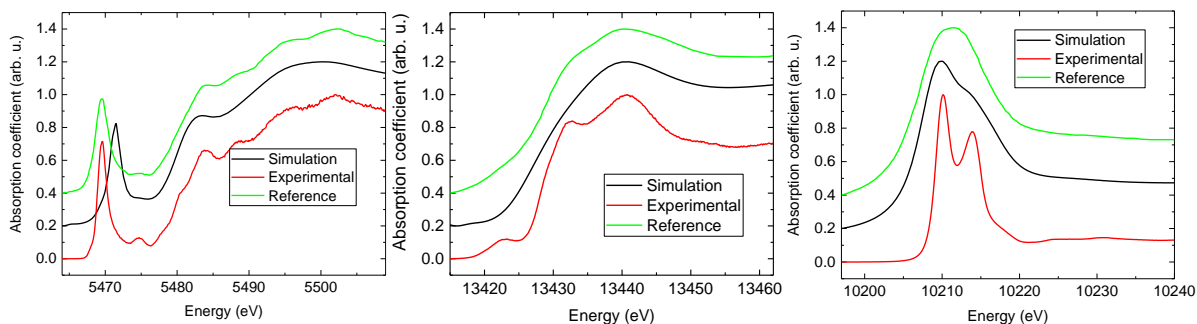
Figure 3. Experimental HERFD-XANES, simulated and literature XANES for (from left to right) V K, Bi and W L$_3$ edges.

Wide area scanning electron microscopy (SEM) (see Figure 4 (C)) of the WO$_3$/BiVO$_4$ thin films reveal a quite homogeneous film composed by roughly spherical nanoparticles. At first glance, larger particles are embedded in a crust composed of smaller structures. FTO, whose large micrometric crystals have a characteristic irregular shape, is not evident, indicating a good coverage of the ohmic support by the photoactive material. AFM analysis confirms the morphological results obtained by SEM. Cross sections, taken along random directions where the large nanoparticle morphology could be more easily distinguished, reveal height variations of the order of 5-10 nm (Figure 4 B) consistent with a smooth surface which explains the good transparency of the thin films showed in Figure 1. Along the red arrow in figure 4 A, showing a 0.5 x 0.5 µm detail of the WO$_3$/BiVO$_4$ surface, one intercepts quite clearly a sequence of four large particles, which can be observed in the depth analysis of Figure 4 (B) (red line) as four humps centred at about 40, 80, 170 and 220 nm, indicating particle diameters of the order of 40-50 nm. Comparatively smaller particles, also roughly spherically shaped, with diameters of 10-20 nm are evident in Figure 4 (A) (AFM topography): these particles randomly fill the gaps between the larger particles and cover the underlying ones. The comparison with previous AFM data reported for the same type of WO$_3$ substrates[17] indicates that the larger particles are essentially constituted by WO$_3$, consistent with their relatively monodisperse average size of ca. 50 nm, (Figure S2) whereas the finer grains which surround and coat the underlying large particles are assigned to electrodeposited BiVO$_4$. The intimate contact between WO$_3$ and BiVO$_4$, a prerequisite for efficient sensitization upon visible light excitation, is thus fulfilled.

Photoelectrochemical measurements reported in the next section will show that, despite the finer size of the BiVO$_4$ particles filling the interstices between the WO$_3$ ones, electrolyte permeation of the nanocrystalline film is still possible, guaranteeing effective hole scavenging pathways.
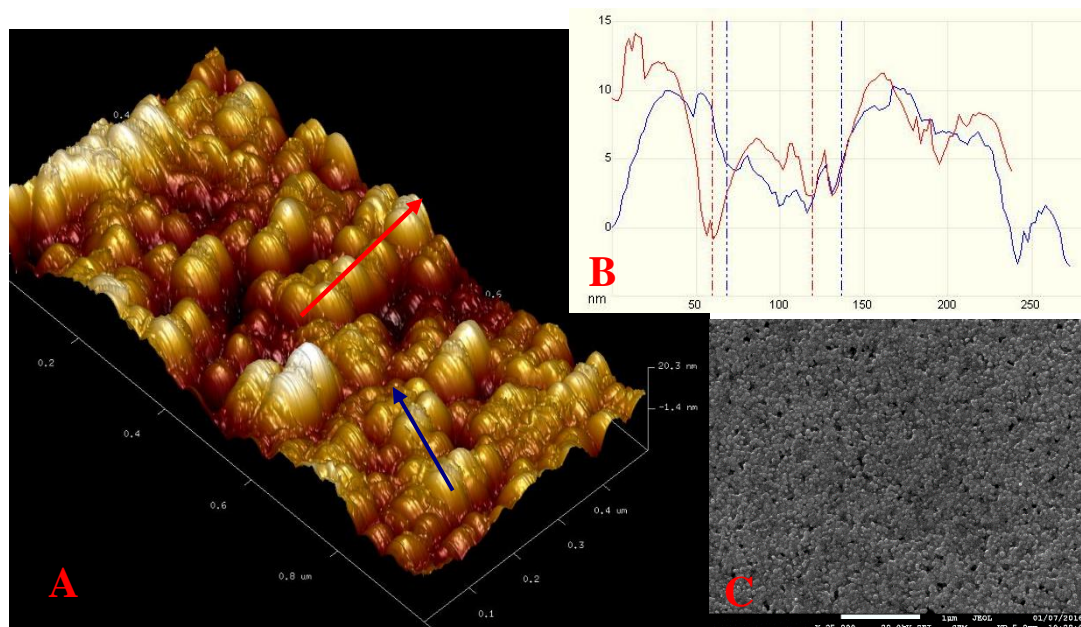
Figure 4. (A) (0.5 x 0.5 µm) AFM topography of $WO_3/BiVO_4$ films following 500 C° annealing. Arrows represents sampling directions along which depth profiles (B) (blue and red) were taken. (C) Large area (5 x 5 µm) SEM image showing the good surface homogeneity and coverage of the photoactive material

3.2 General Photoelectrochemical properties of $WO_3/BiVO_4$ heterojunctions

Scheme 1 depicts the simplified mechanism of operation of a photoelectrochemical cell based on n-n $WO_3/BiVO_4$ under visible light with $\lambda > 450$ nm and front (through the electrolyte) illumination, a condition frequently adopted for this work. Under such circumstance WO_3 absorbs a negligible amount of radiation while photocarrier generation occurs mostly within the sensitizing $BiVO_4$ layer which is able to undergo ultrafast electron transfer to WO_3.[24, 40] Recombination involving holes left within $BiVO_4$ and electrons trapped in WO_3 can survive beyond the microsecond time scale, consistent with a favourable competition between charge separation and recombination. Hole lifetimes of few microseconds are actually deemed insufficient to drive complex multi-electron reactions, like those of frequent interest in redox catalysis, however Durrant et al. showed that holes in $BiVO_4$ can survive up to the 1 s scale with increasing anodic bias,[41] leaving sufficient time to drive kinetically demanding redox reactions, like water oxidation, constituting the prominent hole scavenging pathway in the presence of inert electrolytes. Electrons, under either chemical or electrical potential gradient are driven to the catalytic counter electrode (Pt), where, in aqueous solution, hydrogen is the main reduction product. Thus, the principal difference between photoelectrocatalysis and photocatalysis is that electrons, being unable to reside in the semiconductor, where they could otherwise accumulate under illumination at open circuit, are not available for the reductive formation of active oxidizing intermediates, like superoxide and peroxide species formed by reduction of

11

oxygen. However, since recombination is greatly retarded under anodic bias, the main pollutant degradation mechanism likely to occur at the illuminated n-type semiconductor in a photoelectrochemical cell, involves a flux of long lived holes which may intercept the pollutant directly interacting with the semiconductor surface. Alternatively, the degradation mechanism can be mediated or complemented by strong oxidizing species like H_2O_2 and $\cdot OH$, generated upon primary water oxidation.
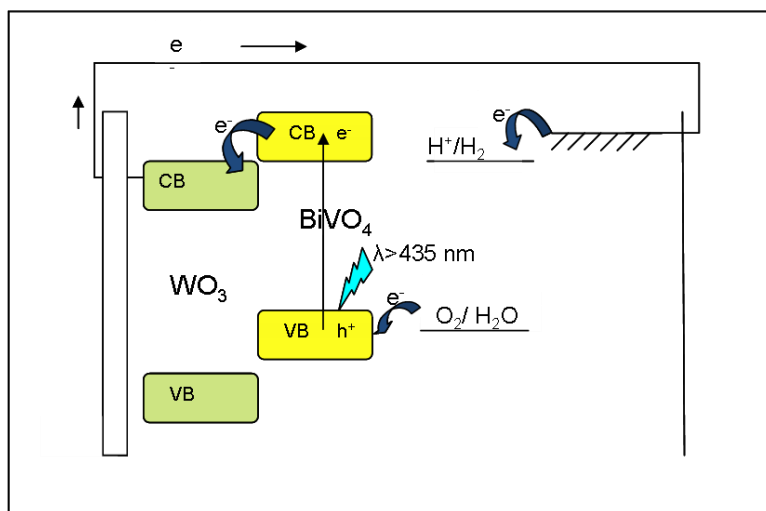
Scheme 1. Schematic operation of a photoelectrochemical cell constituted by a $WO_3/BiVO_4$ n-n photoanode connected to a metal counter electrode under $\lambda \geq 450$ nm illumination and applied reverse bias (positive at the photoanode, negative at the cathode).

The J/V curve of $WO_3/BiVO_4$ in aqueous 0.5 M Na_2SO_4 at neutral pH is consistent with the n-type properties of the junction with photocurrent steadily increasing with increasing anodic bias until reaching a limiting value > 2.5 mA/cm^2 at ca. 1.4 V vs SCE (Figure 5 (A), red line), which represent the maximum rate of hole transfer to the electrolyte under our experimental conditions. Within the potential interval 0-1.5 V vs SCE the dark current (blue line in figure 5 (A)) is negligible, except for a faradaic wave centred at ca. 0.1 V vs SCE and assigned to the re-oxidation of W^{5+} of WO_3, which is generated when the cell is switched on at negative voltages. $WO_3/BiVO_4$ delivers ca. twice the current generated by a reference WO_3 film (Figure 5 (A), black line) under identical conditions, in agreement with the better light harvesting properties of the heterojunction, confirmed by the IPCE spectrum recorded at 1.5 V vs SCE (Figure 5 (B)). Conversion of photons to electrons in $WO_3/BiVO_4$ starts at 510 nm, consistent with a 2.4 eV band gap and reaches a maximum of ca. 45 % at 460 nm, where the photoconversion of WO_3 is just at the very beginning; a secondary peak is observed at 410 due to the overlapping contribution of $BiVO_4$ with WO_3, exhibiting a shoulder at that wavelength, followed by a third peak in the UV, around 360 nm which is determined by the maximum

photoactivity of WO$_3$, characterized by an IPCE peak at the same wavelength (Figure 5 (B), black line). Clearly, at this wavelength, the optical excitation of the two materials is not selective and charge separation occurring within WO$_3$ may result in either hole transfer to the nearby electrolyte or downhill to the valence band of BiVO$_4$ from which the final transfer to the electrolyte occurs. Overall, the WO$_3$/BiVO$_4$ junction covers, with an average 45 % quantum yield the 360-460 nm range.
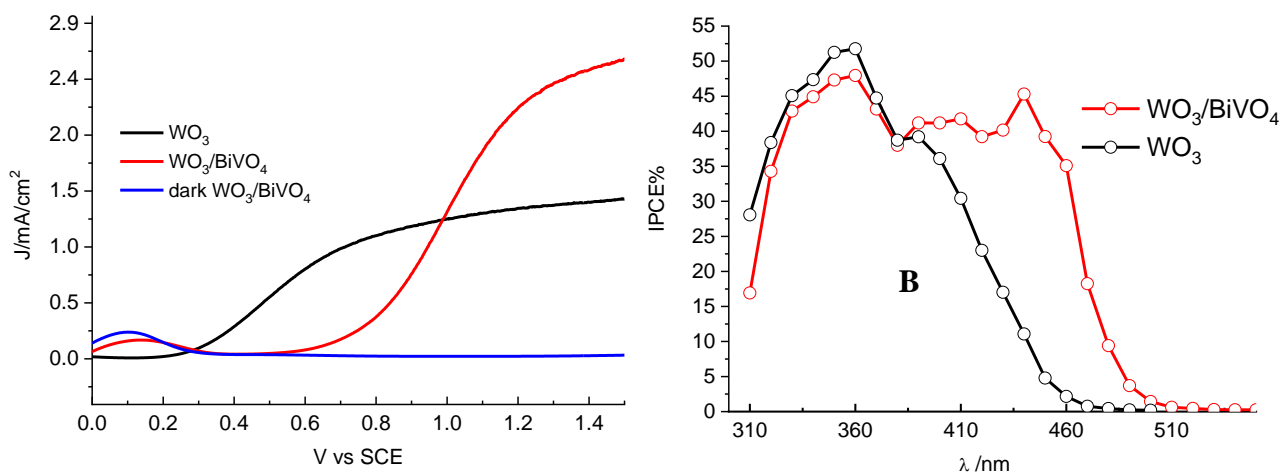
Figure 5. (A) J/V curves of WO$_3$/BiVO$_4$ compared to WO$_3$ under 0.1 W/cm^2 AM 1.5 G illumination. (B) Comparative IPCE spectra taken at 1.5 V vs SCE. In this case front side (from the electrolyte) illumination was adopted. 0.5 M Na$_2$SO$_4$ at pH 7.

IPCE recorded in backside illumination, through FTO and WO$_3$, preserves the magnitude of the photoconversion peak at 460 nm, determined uniquely by the photoresponse of BiVO$_4$ (Figure 6 (A)). This indicates that electron transport through the film is, upon BiVO$_4$ excitation, equally effective regardless of whether photocharge is generated close to the FTO (back illumination mode) or at the maximum distance from the electron collector. In order to explain this evidence, we have to assume a substantially homogenous interpenetration between the electrodeposited BiVO$_4$ phase and WO$_3$. Indeed, only in this case, irrespective of the illumination geometry, we would obtain a good electron transport, realized through WO$_3$, which acts as the electron transporting layer upon injection by BiVO$_4$, with whom it is always in an intimate contact. It is also interesting to note that the 360 nm peak, where the contribution of the light absorption by WO$_3$ is stronger (ca. 70% of the total absorbance at 360 nm), is, under back side illumination, decreased by a factor of ca. 1/3. This is ostensibly due to a lower hole transfer capability of the innermost WO$_3$ layer (that closest to FTO), probably due to a less effective permeation by the electrolyte and to screening by surrounding BiVO$_4$. Nevertheless the AM 1.5 G solar irradiance between 300 and 360 nm is fairly small, and, under solar

simulated illumination, only a marginally decreased photocurrent is observed from J/V curves collected by changing the thin film excitation conditions under solar simulated illumination (Figure 6 (B)), demonstrating that the composite photoanode could be employed under different illumination geometries, depending on the preferred cell arrangement, with a substantial preservation of its efficiency.
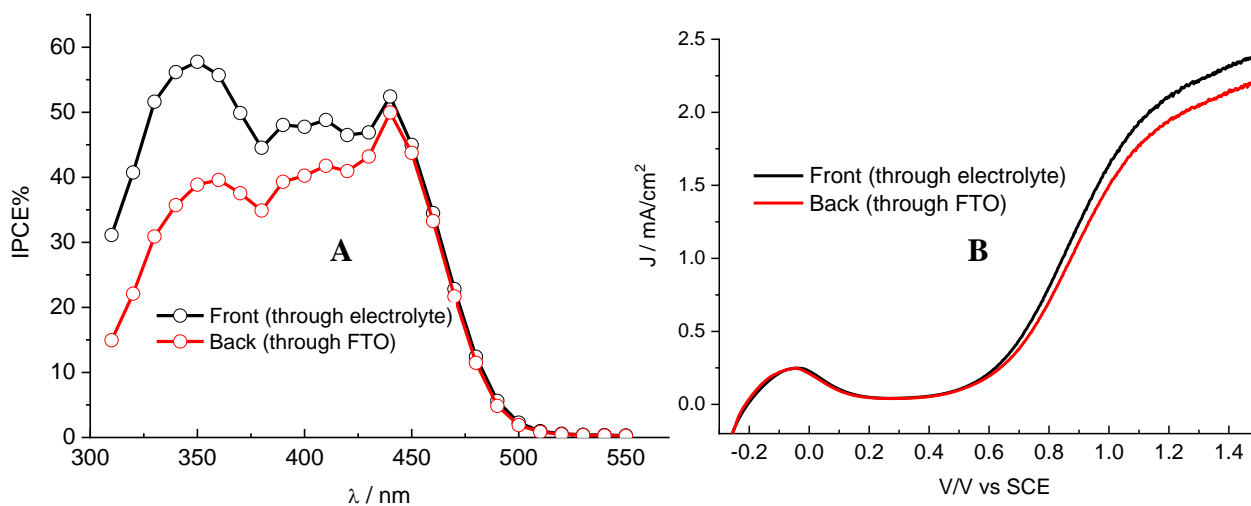

Figure 6. (A) IPCE spectra recorded under different illumination geometries: through electrolyte (black) and through FTO (red). (B) Corresponding J/V curves under AM 1.5 G. 0.5 M Na_2SO_4 at pH 7.

In order to extract information on the oxidation products, generated at WO_3/$BiVO_4$ junctions under illumination in the neutral Na_2SO_4 electrolyte, oxygen detection experiments were performed: in generation/collection experiments, the photoanode is sandwiched against a collector electrode, made of bare FTO, polarized, via a bipotentiostat, at -0.65 V vs SCE. At this voltage, reduction of oxygen evolved at the illuminated semiconductor occurs, and its quantitation is straightforward on the basis of the Faraday laws. Given that molecular oxygen has to diffuse through a fairly small distance, in our case ca. 200 µm, corresponding to the thickness of the sealant which separates the generator from the collector electrode, its detection is fast and the escape of gaseous products into the atmosphere before quantitation can be largely prevented. Clearly, these experiments were conducted under relatively small current densities, to avoid saturation of the inter-electrode spacing with gas bubbles which would otherwise electrically insulate the photoelectrochemical cell. Figure 7 (A) shows the photocurrent response of the sandwich cell, where WO_3/$BiVO_4$ is illuminated under 0.6 V vs SCE, delivering a steady state photoanodic current of ca. 0.25 mA/cm^2 (black line), established a few seconds after light is switched on. Correspondingly, at the collector, the cathodic current determined by oxygen reduction rises, and reaches a constant plateau after ca. 150 s. This reductive current is

maintained, with a profile specular to the photoanodic current, until light is switched off, after 400s of illumination. At this stage, the reductive current drops slower than the photoanodic one, due to the progressive consumption of oxygen accumulated in the electrolyte during the illumination cycle and relaxes to 0 mA/cm^2 approximately 100 s after the establishment of dark conditions. Integration of the respective i/t curves affords a faradaic yield for oxygen evolution of 88 %, confirmed by subsequent measurements at 0.65 V vs SCE anodic bias (87 %), where photocurrent was nearly twice as large (Figure S3). Bulk detection of oxygen, produced under galvanostatic photoelectrolysis (0.5 mA/cm^2 delivered at a voltage of ca. 0.65 V vs SCE) was independently confirmed with a commercial oxygen sensing electrode. Detection of oxygen in the bulk demanded longer illumination times, extending up to 1 hour, during which oxygen progressively saturates 30 ml of electrolyte, initially purged with N$_2$. The rate of oxygen production, at least initially, is similar to or even faster than that observed with an IrO$_2$ anode biased at the same current density (Figure 7 (B)), however, with the photoanode, the final concentration of oxygen attained after 1 hour illumination is lower by ca. 25 %. Treatment of the photoelectrolyzed solution with iodide, led to the formation of I$_3^-$, diagnostic of the presence of H$_2$O$_2$ as a secondary oxidation product of water, (Figure S4) consistent with the < 100 % yield observed in generation/collection experiments in the thin layer cell. Thus, differently from WO$_3$, which, in sulphate based electrolytes, produces mainly persulfate anions as a consequence of the reaction of SO$_4^{2-}$ with photo-generated OH radicals,[42] oxygen is the most representative water oxidation product at the illuminated BiVO$_4$/electrolyte interface, indicating that the mechanism of water oxidation takes probably place through concerted multi-electron reactions which do not involve mono-electronic radical intermediates. We would like to recall that in the WO$_3$/BiVO$_4$ junction, even in the presence of direct excitation of WO$_3$, hole transfer to BiVO$_4$ is energetically favourable, resulting in the population of the valence band of the latter which is thus the main actor in the subsequent photoanodic reactions. The more than 300 mV cathodic shift recorded in weak base buffers (either composed of phosphate[43] or borate), (Figure S5) associated to rapid oxygen evolution (Figure S6) and lack of peroxide intermediates at least within the sensitivity of the spectrophotometric test with iodide, (Figure S7) corroborates the indication of a complex mechanism for oxygen evolution, probably involving Proton-Coupled-Electron Transfers (PCET) which can be conveniently catalysed by weak bases, as observed in the case of other oxygen evolving junctions like TiO$_2$/Co-pi.[44]

Finally, spin trap EPR spectra recorded with BiVO$_4$ powder revealed no presence of OH radical intermediates (Figure S8 (A)) which, instead, are clearly observed with the WO$_3$ powder under otherwise identical conditions (Figure S8 (B)), showing the appearance of the characteristic 1:2:2:1 quartet associated to the formation of DMPO-OH· where the N and H nuclei exhibit the same

hyperfine coupling constant with the unpaired electron.[45, 46] This observation is consistent with Saison et al.[1] who did not practically observe the photo-production of OH radicals with $BiVO_4$ despite very intense UV illumination and the fact that the estimated valence band edge of $BiVO_4$ should make OH radical formation weakly exoergic; kinetic barriers may thus render this reaction prohibitively slow compared to other water oxidation pathways.

From these observations we conclude that in order for contaminant degradation to be effective with $BiVO_4$ based materials, one has to rely either on the direct oxidation of the organics interacting with the semiconductor surface, or on their reaction with H_2O_2 (or its decomposition by products, among which OH radicals) which slowly accumulates as a product of incomplete water oxidation in certain electrolytes.
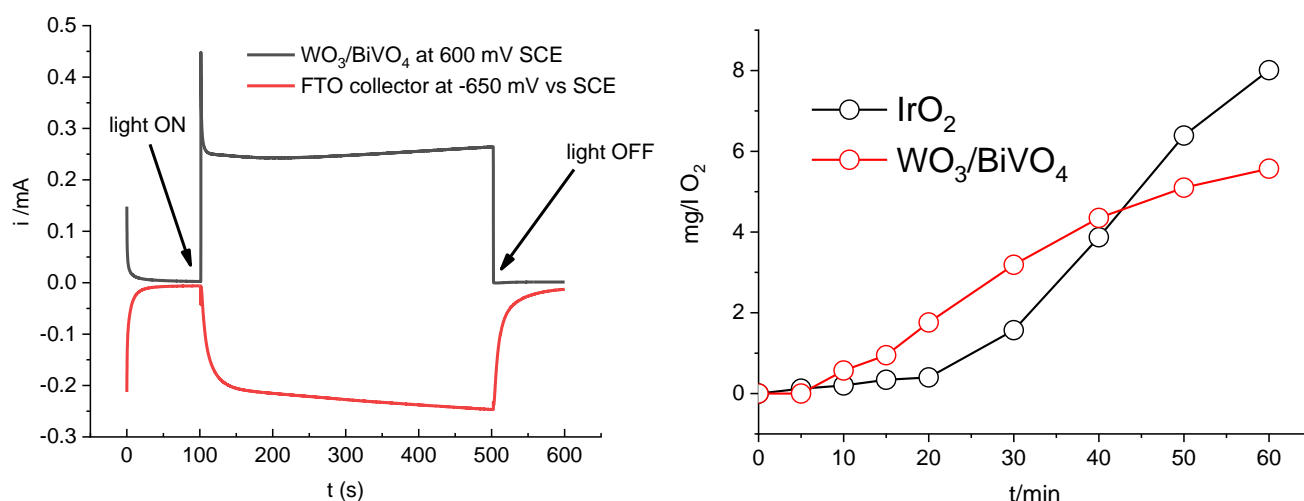
Figure 7. (A) Oxygen detection with a generator/collector assembly, where the oxygen generator is the $WO_3/BiVO_4$ photoanode. (B) Bulk oxygen detection under prolonged galvanostatic (J=0.5 mA/cm^2) photoelectrolysis, compared to an IrO_2 electrode biased at the same current .

In view of our intended application to water remediation processes, we have thus selected the Na_2SO_4 electrolyte, where the generation of some H_2O_2 can cooperate to the oxidative degradation of organic species. Besides this, sulfate salts are ubiquitous electrolytes in the majority of natural waters, in a wide range of concentrations, from thousands to tens mg/l, with the highest concentrations commonly found in subterraneous waters. Thus, the use of Na_2SO_4 also simulates conditions which can be effectively found when extending the photoelectrocatalytic remediation process to real samples. The capability of the $WO_3/BiVO_4$ to oxidize organic substances under illumination was initially evaluated with species like alcohols (methanol) and different carboxylate salts (formate and citrate buffers). Consistent with reduced recombination, the presence of organic hole scavengers leads to an anticipated photoanodic onset (at least 300 mV or higher) with respect to inert electrolytes (Figure

16

S9). A general enhancement of the photocurrent of at least a factor of 1/3 is also present. The largest improvement in photocurrent is observed in the presence of citrate, which, among the selected species is the easiest to oxidize and ostensibly the best scavenger of the series. Compared to inert electrolytes like sodium sulfate or sodium perchlorate, the photocurrent in citrate buffer is more than doubled, suggesting a photocurrent doubling mechanism due to injection by sufficiently reducing citrate radical intermediates. Unfortunately, the limited stability of $BiVO_4$ in citrate buffer, probably due to dissolution caused by Bi^{3+} complexation by citrate, prevented sufficiently accurate IPCE measurements in that electrolyte. In the presence of optimized charge separation, the onset of the J/V curves provides a conservative estimate of the flat band potential of the n-n junction under investigation. The value of -0.3 V vs SCE, extracted from the blue line of Figure S9 is in reasonable agreement with the ca. -0.4 V vs SCE value provided by Grigioni et al.[40] who used redox probes for flat band determination. It has also to be considered that the flat band potential of the n-n junction might depend on the preparation route, which, inducing variable doping and defect densities ultimately control the Fermi levels of the two materials and, as a consequence, the one attained following electronic equilibration upon junction formation. Slightly different flat band levels could thus be expected in junctions prepared according to different methodologies. Finally, IPCE spectra measured under sufficiently stable conditions, in the presence of sacrificial agents like methanol and sodium formate, confirm the improved hole scavenging by the organics with respect to inert electrolytes and allow to quantify the charge transport efficiency of the junction, which, at a level of ca. 70% (Figure S10) at the saturation bias (1.2 V vs SCE), was found quite satisfactory.

In order to test the efficiency of WO3/BiVO4 heterojunctions in advanced oxidation process for the degradation of contaminants of emerging concern in water, two target compounds, namely ketoprofen (KTP) and levofloxacin (LFX) were selected. These compounds have been chosen for the same reasons already discussed in Ref. , where the degradation pathway of both these molecules subjected to photo-electrochemical treatment with WO_3 photoanodes was also reported. It is therefore possible to compare the performance of $WO_3/BiVO_4$ heterojunctions with respect to those of pristine WO_3.

3.3 Photoelectrochemical degradation of KTP and LFX at $WO_3/BiVO_4$ heterojunctions

Figure XX reports the J/V curves $WO_3/BiVO_4$ in neutral 0.5 M Na_2SO_4 the presence of either 10^{-3} M KTP (Figure 8 (A)) or 10^{-2} M LFX (Figure 8 (B)) recorded under AM 1.5 G. While in these experiments the drug concentration was unrealistically high compared to the typical concentration of emerging contaminants in natural waters (few ppm), these J/V curves are intended to show whether an interaction of the selected pharmaceuticals with the $WO_3/BiVO_4$ surface could be established. The evidence is generally positive: as a result of the hole scavenging processes by the organic species, the

photoanodic onset is cathodically shifted, and, particularly in the activation region of the curve between 0.2 and 0.4 V (inset of figure 8 (A)), the photocurrent is enhanced, with a good matching with the photocurrent transients recorded by chopping the illumination source. While this effect is already evident with 10^{-3} M KTP, it is totally obvious in the case of LFX, which, besides, being 10 fold more concentrated, it is also an easier to oxidize species. Indeed in this latter case, the photoanodic current is already evident at negative voltages, accounting for a cathodic shift of at least 500 mV with respect to the reference blank electrolyte. Interestingly, the dark electrochemical response of LFX, appearing as a broad wave centred around 0.9 V vs Pt (ca. 0.3 V vs SCE) at FTO/WO$_3$ electrodes[18] is here not observed (black line Figure 8 (B)), probably due to coverage and passivation of the uncoated FTO back contact by the small BiVO$_4$ particles.
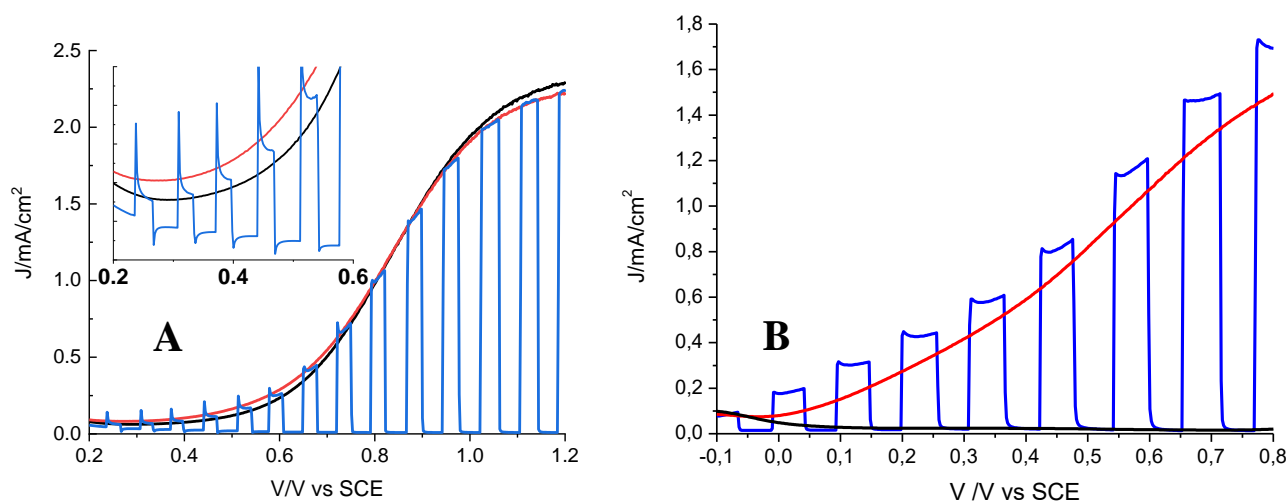
Figure 8. Steady state and shuttered J/V curves under AM 1.5 G of WO$_3$/BiVO$_4$ in neutral 0.5 M Na$_2$SO$_4$ in the presence of 10^{-3} M KTP (A) and with 10^{-2} M LFX (B). For each drug, the saturation concentration in the chosen electrolyte was used. In (A) the JV curve of the same photoanode in the blank Na$_2$SO$_4$ electrolyte was given as a reference.

Figure 9 shows the photoelectrochemical degradation test of either KTP or LFX under various conditions in a two electrode cell with a platinum counter electrode. Generally, 0.7 mM Na$_2$SO$_4$ electrolyte was used, to simulate the average salinity of real freshwater[28]. Nevertheless tests carried out with higher Na$_2$SO$_4$ concentrations, up to 0.1 M, did not show a significant dependence of the degradation rate on the supporting electrolyte concentration. From Figure 9 (A), taken at a bias of 1.2 V vs Pt, it can be observed that a significant degradation of KTP occurs already under $\lambda \geq 450$ nm excitation which leads to the abatement of ca. 35% of the initial drug concentration after 5 hours. Unsurprisingly, due to the small light harvesting for $\lambda \geq 450$ nm, a pure WO$_3$ film is, under identical conditions, scarcely active, achieving ca. 10 % degradation after a comparable time. The

photoelectrochemical abatement is clearly accelerated by shining on $WO_3/BiVO_4$ the entire visible spectrum, starting from 400 nm, leading to the disappearance of more than 60 % of the drug. Consistent with the indications extracted from the J/Vs, LFX is easier to oxidise, with more than 80% degradation found after 5 hours under visible (> 400 nm) illumination and 1.5 V vs Pt . To rule out possible spurious effects due to direct electrochemical degradation of LFX at such anodic potential, we biased the photoanode at 0.4 V vs Pt, a potential at which the dark electrochemical response of LFX is negligible,[18] but the photoanodic response of the $WO_3/BiVO_4$ is sizable, albeit not optimal. Still, despite the small bias, LFX photoelectrochemical degradation occurs, although at a slower rate, achieving ca. 50% abatement after 5 hours.
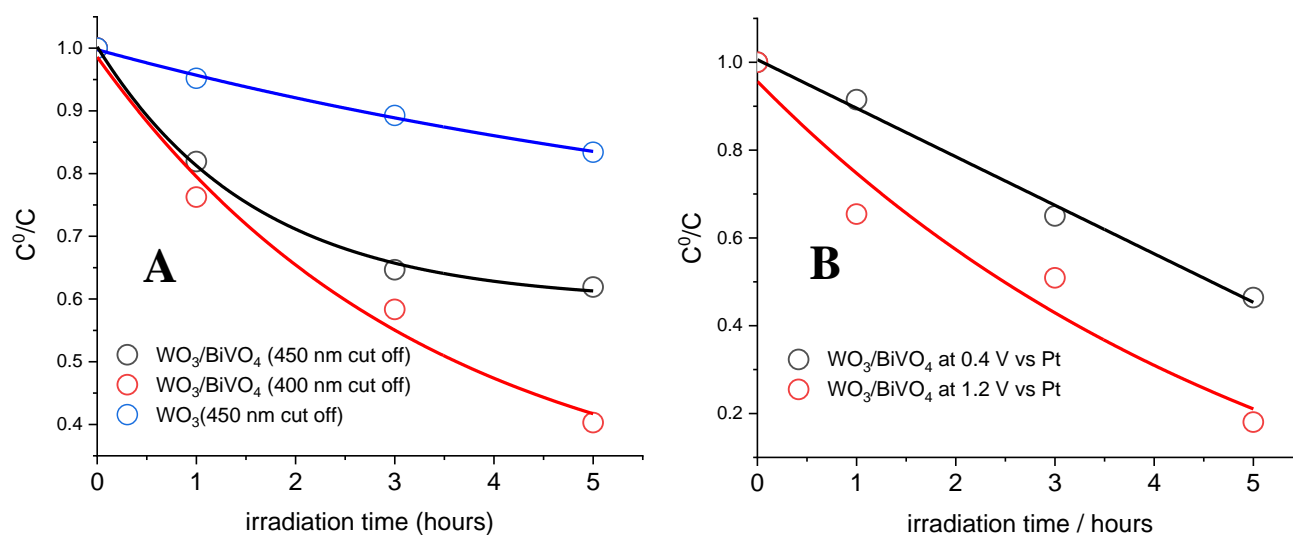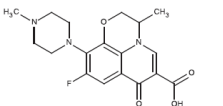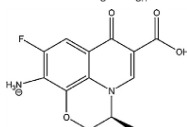
Figure 9. Photoelectrochemical Degradation kinetics of 10 ppm KTP (A) and LFX (B) in 0.7 mM Na_2SO_4. In (A) the photoelectrolysis was carried out at pH 7 biasing at 1.2 V vs Pt under AM 1.5G with 450 (black) and 400 nm cut off filters (red). In (B), two different anodic biases were tested: 0.4 V vs (black) and 1.5 V (red) vs Pt at pH 6.
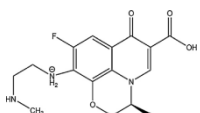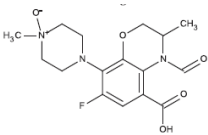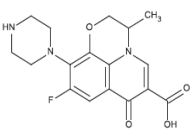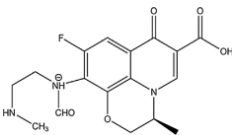
The main degradation products of LFX generated upon photoelectrolysis with $WO_3/BiVO_4$ were identified and their fate monitored up to 16 hours of illumination. The structural assignments of the intermediates were done on the basis of the comparison of the fragment ions detected in the MS-MS spectra with those reported in previous studies. [47, 48]

Concerning LFX, in addition to the parent molecule, five intermediate products were identified (Table 1) in the withdrawal solutions obtained during photoelectrochemical degradation. These compounds have molecular ions at m/z 336, 279, 338, 348 and 364. All of them correspond to protonated molecular species $[M+H]^+$. These compounds are essentially identical to those previously found after

photoelectrolysis with WO_3 photoanodes:[18] the product with m/z 279 can be attributed to the oxidation of the piperazine side-chain. [49] The intermediate with m/z of 364 possibly derives from the ring-opening at the N1 position (see chart 1) followed by further oxidation.[50] The fragment at m/z 348 may derive from demethylation (-14 Da) of the parent compound having m/z 362.[50] The exact concentrations of the intermediates have not been quantified since the corresponding standards for calibration are not commercially available. However, the relative abundance can be approximately estimated from their associated peak integral. Figure 10 (B) shows that the abundances of the intermediates decrease with time, however compared to what was observed for LFX oxidation at WO_3 photoanodes, the intermediate m/z 364 peak area is here still significant (more than three times the instrumental background noise) after 10 h of photoelectrolysis, indicating a lower efficiency of $WO_3/BiVO_4$ in the oxidation of LFX intermediates. Additionally, from a qualitative point of view, by comparing data in Figure 10 with those reported in Fig. 11 of Ref. [Catalysis Today], it seems that the intermediate degradation process is slower than that recorded with β25 modified WO_3 photoelectrodes under analogous conditions (except that λ≥380 nm illumination was used with β25/WO_3).

Table 1. Degradation products of LFX upon photoelectrochemical treatment with $WO_3/BiVO_4$ at 0.4 V vs Pt and λ > 400 nm illumination

Precursor ion	Tr	MS^2	Structure
362	7.18	362 318	
279	9.79	261	
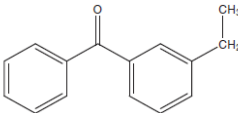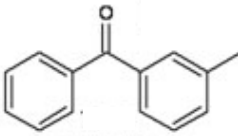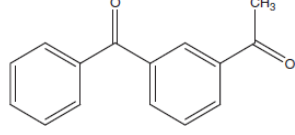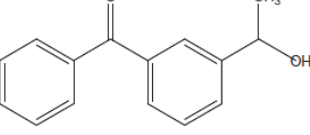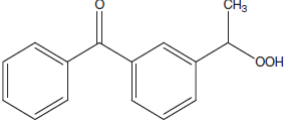
336	6.96	261	
		235	
338	4.48	320	
		310	
		294	
		292	
348	7.10	304	
		284	
		261	
364	6.51	346	
		333	
		289	
		261	
		235	

In the case of the degradation of KTP, the most abundant intermediates observed have m/z 243, 227, 225, 212 and 211 (see Table 2).

As already reported[51] the first degradation step of degradation seems to be the decarboxylation, this is confirmed by the fact that the most significant fragment correspond to m/z 211. The structural assignment of the precursor ion was performed on the basis of the comparison of the m/z fragments with literature data.[52] The m/z 212 intermediate is consistent with 3-hydroxymethyl-benzophenone, and the fragment analysis of m/z 227 and 225 intermediates leads to 3-acetylbenzophenone and 3-hydroxylmethyl benzophenone. Differently to what observed in REF. [catalysis] a fragment corresponding to a hydroperoxide derivative m/z 243 has been detected. The peak area of the fragments vs. irradiation time is reported in Figure 10, where it can be observed that most of the KTP degradation by products maintain a nearly constant concentration, even by prolonging photoelectrolysis up to 15 hours. Again, this is different from what observed with WO_3, where the degradation of these intermediates, triggered by OH radicals, progressed towards mineralization. This is explained with the insufficient oxidizing capability of $BiVO_4$ which has to rely on the direct oxidation of the organics interacting with the surface, rather than on a photogenerated flow of OH radicals which are known to abstract H from most of the C-H bonds, resulting in the progressive formation of oxygenated species in aqueous solution. Thus, stable molecules without easily oxidazable groups, like those intermediates reported in table 2 may survive for long times at the illuminated $BiVO_4$ surface. Moreover, the amount of H_2O_2 produced during the photoelectrolysis as a result of incomplete water oxidation is probably too low in concentration, at

least in our conditions, to constitute a significant source of OH radicals at least for experiments of the duration of a few hours.

Table 2. Degradation products of LFX upon photoelectrochemical treatment with $WO_3/BiVO_4$ at 0.4 V vs Pt and $\lambda > 400$ nm illumination

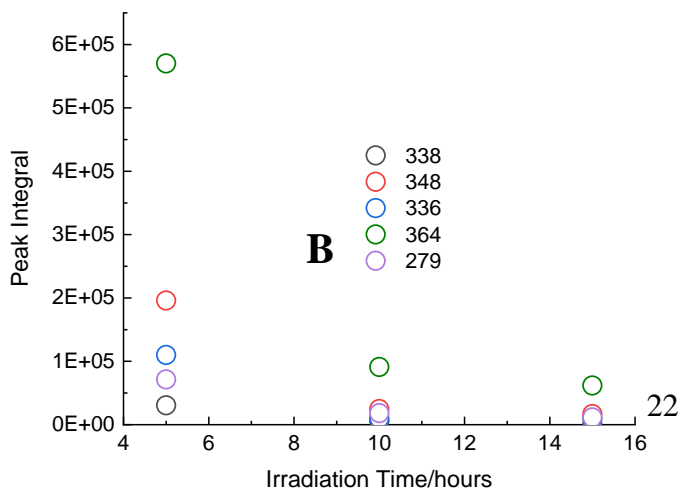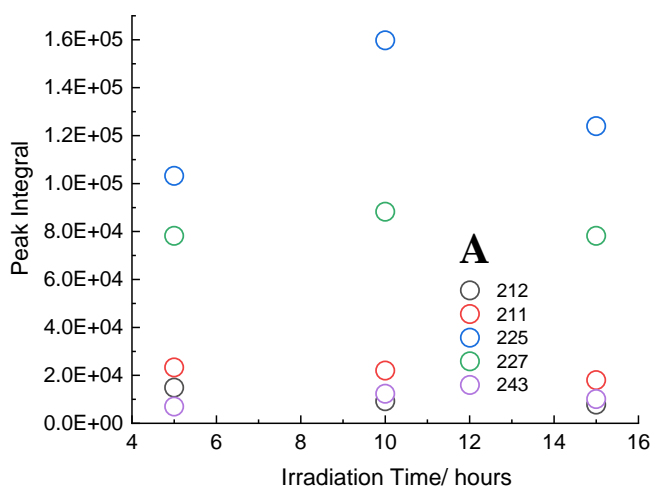| Precursor Ion	Tr	MS^2	Structure
211	14.35	105	
212	17.17	196 182 183 154	
225	15.48	183 147 105	
227	13.59	150 183 209	
243	10.69	225 199 120	

A

B

Figure 10.   Degradation kinetics of oxidation intermediate produced during photoelectrolysis of KTP (A) and LFX (B). Conditions are the same as those reported for Table 1 and 2 respectively.

4. Conclusions

In this work we have considered the environmental application of $WO_3/BiVO_4$ films obtained by electrochemical deposition of $BiVO_4$ over mesoporous WO_3. These n-n junctions are   characterized by an interpenetrated morphology where small $BiVO_4$ nanoparticles embed larger WO_3 nanostructures, resulting in the intimate contact between these two materials. Consistently, electron transfer from $BiVO_4$ to WO_3 occurs with a good efficiency, leading to electron collection efficiencies of the order of 70 % in presence of appropriate hole scavengers, with a spectral response extending in the visible up to 500 nm. Injection from $BiVO_4$ into WO_3 results in a population of holes in the valence band of $BiVO_4$, which can be directed, under applied bias, to the semiconductor/electrolyte interface, where they trigger oxidation reactions. In inert aqueous electrolytes, the main oxidation product obtained at illuminated and biased $WO_3/BiVO_4$ is oxygen. A minor amount of H_2O_2 is found in sodium sulfate electrolytes, but not in the presence of weak bases, which improve the rate of oxygen evolution probably through PCET reactions at the $BiVO_4$ surface. The negative evidence for production of OH radicals, known to be effective intermediates in promoting the oxidation of the large majority or organic species, restricts the application of $WO_3/BiVO_4$ to photoelectrochemical remediation processes where the pollutants are relatively easy to oxidize species which can react directly with photoinduced holes at the $BiVO_4$/electrolyte interface. The example provided by LFX shows that in this case drug degradation, up to probable mineralization could be effectively achieved at $WO_3/BiVO_4$ junctions after sufficiently prolonged illumination times. The same is however not true for KTP: although the parent compound could be degraded in a significant percentage, some of its decomposition byproducts, being stable aromatic species, were found to be persistent in aqueous solution during an experiment of the duration of 16 hours. Despite better solar harvesting, the employment of $WO_3/BiVO_4$ in photoelectrochemical environmental remediation processes is thus much less universal than that possible with wider band gap semiconductors like TiO_2 and WO_3

Aknowledgements

References

1.   T. Saison, N. Chemin, C. Chaneac, O. Durupthy, L. Mariey, F. Maugé, V. Brezovà and J.-P. Jolivet, *J.Phys.Chem. C*, 2015, **119**, 12967-12977.
2.   F. F. Abdi and R. Van de Krol, *J.Phys.Chem. C*, 2012, **116**, 9398-9404.
3.   J. Su, L. Guo, S. Yoriya and C. A. Grimes, *Crystal Growth & Design*, 2009, **10**, 856-861.
4.   Q. Jia, K. Iwashina and A. Kudo, *PNAS*, 2012, **109**, 11564-11569.
5.   M. Oshikiri, M. Boero, J. Ye, Z. Zou and G. Kido, *J.Chem.Phys.*, 2002, **117**, 7313-7318.
6.   B. Zhou, X. Zhao, H. Liiu, J. Qu and C. P. Huang, *Sep.Purif.Technol.*, 2011, **77**, 275-282.
7.   N. C. Castillo, L. Ding, A. Heel, T. Graule and C. Pulgarin, *J.Photochem.Photobiol.A: Chemistry*, 2010, **216**, 221-227.
8.   M. Long, W. Cai, J. Cai, B. Zhou, X. Chai and Y. Wu, *J.Phys.Chem. B* 2006, **110**, 20211-20216.
9.   M. Shang, W. Wang, S. Sun, J. Ren, L. Zhou and L. Zhang, *J.Phys.Chem. C*, 2009, **113**, 20228-20233.
10.   H. Li, H. Yu, X. Quan and H. Zhao, *Adv.Funct.Mater.*, 2015, **25**, 3074-3080.
11.   R. Li, H. Han, F. Zhang, D. Wang and C. Li, *Energy Environ. Sci*, 2014, **7**, 1369-1376.
12.   H. Li, Y. Sun, B. Cai, S. Gan, D. Han and L. Niu, *Appl.Catal.B: Environmental*, 2015, **170-171**, 206-214.
13.   F. Chen, Q. Yang, J. Sun, F. Yao, Y. Wang, X. Wang, X. Li, C. Niu, D. Wang and G. Zeng, *ACS Appl.Mater.Interfaces* 2016, **8**, 328877-332900.
14.   K. Sayama, A. Nomura, T. Arai, T. Sugita, R. Abe, M. Yanagida, T. Oi, Y. Iwasaki, Y. Abe and H. Sugihara, *J.Phys.Chem. B*
2006, **110**, 11352-11360.
15.   I. Tantis, L. Bousiakou, Z. Frontistis, D. Mantzavinos, I. Konstantinou, M. Antonopoulou, G.-A. Karikas and P. Lianos, *J. Haz.Mat.* , 2015, **294**, 57-63.
16.   I. Tantis, E. Stathatos, D. Mantzavinos and P. Lianos, *J.Chem.Technol. Biotechnol.* , 2015, **90**, 1338-1344.
17.   G. Longobucco, L. Pasti, A. Molinari, N. Marchetti, S. Caramori, V. Cristino, R. Boaretto and C. A. Bignozzi, *Appl.Catal.B: Environmental*, 2017, **204**, 273-228/272.
18.   V. Cristino, G. Longobucco, N. Marchetti, S. Caramori, C. A. Bignozzi, A. Martucci, A. Molinari, R. Boaretto, C. Stevanin, R. Argazzi, M. Dal Colle, R. Bertoncello and L. Pasti, *Catal.Today*, 2018, 10.1016/j.cattod.2018.1009.1020.
19.   B. Zhou, J. Qu, X. Zhao and H. Liu, *J. Environ.Sci.* , 2011, **23**, 151-159.
20.   P. Chatchai, Y. Murakami, S. Kishioka, A. Y. Nosaka and Y. Nosaka, *Electrochim. Acta*, 2009, **54**, 1147-1152.
21.   P. Chatchai, S. Kishioka, Y. Murakami, A. Y. Nosaka and Y. Nosaka, *Electrochim. Acta*, 2010, **55**, 1147-1152.
22.   J. Su, L. Guo, N. Bao and C. A. Grimes, *Nano Lett.*, 2011, **11**, 1928-1933.
23.   P. Chatchai, A. Y. Nosaka and Y. Nosaka, *Electrochim. Acta*, 2013, **94**, 314-319.

24. I. Grigioni, M. Abdellah, A. Corti, M. V. Dozzi, L. Hammarstrom and E. Selli, *J.Am.Chem.Soc.*, 2018, **140**, 14042-14045.
25. K. H. Ye, Z. Chai, J. Gu, X. Yu, C. Zhao, Y. Zhang and W. Mai, *Nano Energy*, 2015, **18**, 222-231.
26. L. Pasti, E. Sarti, A. Cavazzini, N. Marchetti, F. Dondi and A. Martucci, *J.Sep.Sci.*, 2013, **36**, 1604-1611.
27. M. González-Pleiter, S. Gonzalo, I. Rodea-Palomares, F. Leganés, R. Rosal, K. Boltes and F. Fernández-Piñas, *Water Res.* , 2013, **47**, 2050-2064.
28. https://www3.epa.gov/caddis/ssr_ion_int.html.
29. V. Cristino, M. Sabrina, A. Molinari, S. Caramori, S. Carli, R. Boaretto, R. Argazzi, L. Meda and C. A. Bignozzi, *J. Mater.Chem.A*, 2016, **4**, 2995-3006.
30. J. A. Seabold and K.-S. Choi, *J.Am.Chem.Soc.*, 2012, **134**, 2186-2192.
31. *http://rruff.geo.arizona.edu/AMS/amcsd.php*, *American Mineralogist Crystal Structure Database*.
32. Y. Joly, *Phys.Rev. B*, **63**, 125120-125121-125120-125110.
33. B. D. Sherman, M. V. Sheridan, C. J. Dares and T. J. Meyer, *Anal.Chem.*, 2016, **88**, 7076-7082.
34. M. Bonchio, Z. Syrgiannis, M. Burian, N. Marino, E. Pizzolato, K. Dirian, F. Rigodanza, G. C. Volpato, G. La Ganga, N. Demitri, S. Berardi, H. Amenitsch, D. M. Guldi, S. Caramori, C. A. Bignozzi, A. Sartorel and M. Prato, *Nat.Chem.*, 2018, 10.1038/s41557-41018-40172-y.
35. A. Kudo, K. Omori and H. Kato, *J.Am.Chem.Soc.*, 1999, **121**, 11459-11467.
36. S. Tokunaga, H. Kato and A. Kudo, *Chem.Mater.*, 2001, **13**, 4624-4628.
37. Z. Zai, A. Getsoian and A. T. Bell, *J. Catal.*, 2013, **308**, 25-36.
38. B. J. Trzesniewski, I. A. Digdaya, T. Nagaki, S. Ravishankar, I. Herraiz-Carradona, D. A. Vermaas, A. Longo and S. Gimenez, *Energy Environ. Sci*, 2017, **10**, 1517-1529.
39. S. Yamazoe, Y. Hitomi, T. Shishido and T. Tanaka, *J.Phys.Chem. C*, 2008, **112**, 6869-6879.
40. I. Grigioni, K. G. Stamplecoskie, E. Selli and P. V. Kamat, *J.Phys.Chem. C*, 2015, **119**, 20792-20800.
41. Y. Ma, R. Pendlebury, A. Reynal, F. Le Formal and J. R. Durrant, *Chem.Sci.*, 2014, **5**, 2964-2973.
42. Q. Mi, A. Zhanaidrova, B. Brunschwig, H. B. Gray and N. S. Lewis, *Energy Environ. Sci*, 2012, **5**, 5694-5700.
43. I. Grigioni, A. Corti, M. V. Dozzi and E. Selli, *J.Phys.Chem. C*, 2018, **122**, 13969-13978.
44. R. S. Khnayzer, M. W. Mara, J. Huang, M. L. Shelby, L. X. Chen and F. N. Castellano, *ACS Catal.*, 2012, **2**, 2150-2016.
45. A. Molinari, E. Sarti, N. Marchetti and L. Pasti, *Appl.Catal.B: Environmental*, 2017, **203**, 9-17.
46. L. Pasti, E. Sarti, A. Martucci, N. Marchetti, C. Stevanin and A. Molinari, *Appl.Catal.B: Environmental*, 2018, **239**, 345-351.
47. Y. Gong, J. Li, Y. Zahng, M. Zhang, X. Tian and A. Wang, *J.Haz.Mat.*, 2016, **304**, 320-328.
48. T. Kosjek, S. Perko, E. Heath, B. Kralj and D. Zigon, *Journal of Mass Spectrometry*, 2011, **46**, 391-401.
49. A. S. Maia, A. R. Ribeiro, C. L. Amorim, J. C. Barreiro, Q. B. Cass, P. M. Castro and M. E. Tiritan, *J.Chromatogr.A*, 2014, **1333**, 87-98.
50. I. Michael, E. Hapeshi, J. Acena, S. Perez, M. Petrovic, A. Zapata and D. Fatta-Kassinos, *Science of the Total Environment*, 2013, **461**, 39-48.
51. R. K. Szabo, C. Megyeri, E. Illes, K. Gajda-Schrantz, P. Mazellier and A. Dombi, *Chemosphere*, 2011, **84**, 1658-1663.
52. R. K. Szabo, C. Megyeri, E. Illes, K. Gajda-Schrantz, P. Mazellier and A. Dombi, *Chemosphere*, 2011, **84**, 1658-1663.